

Atomic-scale mechanisms of deformation-induced cementite decomposition in pearlite

Y.J. Li^{a,b,*}, P. Choi^b, C. Borchers^a, S. Westerkamp^a, S. Goto^c, D. Raabe^b, R. Kirchheim^{a,b}

^a *Institut für Materialphysik, Georg-August-Universität Göttingen, Friedrich-Hund-Platz 1, D-37077 Göttingen, Germany*

^b *Max-Planck Institut für Eisenforschung, Max-Planck-Str. 1, D-40237 Düsseldorf, Germany*

^c *Department of Materials Science and Engineering, Faculty of Engineering and Resource Science, Akita University, Tegata Gakuencho, Akita 010-0852, Japan*

Received 4 February 2011; received in revised form 28 February 2011; accepted 8 March 2011

Available online 11 April 2011

Abstract

Pearlitic steel can exhibit tensile strengths higher than 5 GPa after severe plastic deformation, where the deformation promotes a refinement of the lamellar structure and cementite decomposition. However, a convincing correlation between deformation and cementite decomposition in pearlite is still absent. In the present work, a local electrode atom probe was used to characterize the microstructural evolution of pearlitic steel, cold-drawn with progressive strains up to 5.4. Transmission electron microscopy was also employed to perform complementary analyses of the microstructure. Both methods yielded consistent results. The overall carbon content in the detected volumes as well as the carbon concentrations in ferrite and cementite were measured by atom probe. In addition, the thickness of the cementite filaments was determined. In ferrite, we found a correlation of carbon concentration with the strain, and in cementite, we found a correlation of carbon concentration with the lamella thickness. Direct evidence for the formation of cell/subgrain boundaries in ferrite and segregation of carbon atoms at these defects was found. Based on these findings, the mechanisms of cementite decomposition are discussed in terms of carbon–dislocation interaction.

© 2011 Acta Materialia Inc. Published by Elsevier Ltd. All rights reserved.

Keywords: Cold-drawn pearlitic steel wire; Cementite decomposition; Atom probe tomography; Dislocations; Grain boundaries

1. Introduction

Pearlitic steel subjected to a severe plastic deformation (SPD) process such as heavy cold-drawing can exhibit tensile strengths higher than 5 GPa [1] and is therefore the strongest structural bulk alloy known. Despite its great potential for engineering applications (e.g. as suspension bridge cables, tire cords, springs and wires), the correlation between the enormous strength of pearlite and its microstructural evolution during SPD is still a matter of debate. While the tensile strength can be measured with standard

equipment, an understanding of the microstructural evolution is often limited by the resolution of the microscopic technique used, as the mechanisms involved are often of an atomic-scale nature. A typical microstructural change, frequently observed with transmission electron microscopy (TEM), is the refinement of the lamellar structure down to several nanometers upon straining [2–7]. This led to the proposal that the strength and the lamellar spacing follows a Hall–Petch relation [2,8]. In addition to the formation of the nanoscaled filaments, a concurrent decomposition of cementite was observed by performing Mössbauer spectroscopy [9], field ion microscopy (FIM) [3,4,10–14] and atom probe tomography (APT) [3,4,6,7,15–17]. Combined internal friction [18] and Mössbauer [19,20] experiments suggested that 20–50 vol.% of the cementite phase decomposes during deformation at room temperature. Such a decomposition process is reported to increase the average

* Corresponding author at: Max-Planck Institut für Eisenforschung, Max-Planck-Str. 1, D-40237 Düsseldorf, Germany. Tel.: +49 211 6792853; fax: +49 211 6792333.

E-mail addresses: y.li@mpie.de (Y.J. Li), d.raabe@mpie.de (D. Raabe), rkirch@ump.gwdg.de (R. Kirchheim).

carbon concentration in ferrite far above the equilibrium concentration and to invoke an additional strengthening mechanism due to mechanical alloying (with the assumption that the dissolved carbon atoms are homogeneously distributed in the ferrite). However, since the first report on the decomposition of cementite in the 1960s [21], both the exact mechanism of the decomposition process and the location of the dissolved carbon atoms in ferrite are still a subject of controversy.

As reviewed by Gavriljuk [22,23], there are generally two interpretations of cementite decomposition. Gridnev et al. [19,22] proposed that cementite decomposition is due to the much higher binding energy between carbon interstitials and ferrite dislocations (0.75 eV [24]) as compared to the binding energy of carbon atoms in the cementite lattice (0.40–0.42 eV [25,26]). Thus, ferrite dislocations near the interface with cementite drag carbon atoms out of the cementite into the ferrite, forming a Cottrell atmosphere. On the other hand, Languillaume et al. [27] suggested that the increase in free energy, caused by the geometrical thinning of cementite lamellae and the creation of slip steps during wire drawing, destabilizes cementite and promotes its decomposition. A similar thermodynamic model, based on the Gibbs–Thomson effect and a diffusion-controlled dissolution process, was proposed in Ref. [16].

However, as pointed out by Gavriljuk [23], the models of cementite decomposition proposed in the literature still require experimental proof. To date, it has been a great challenge to tackle this issue due to a lack of appropriate high-resolution characterization techniques with sufficient compositional accuracy. APT has been shown to be one of the most powerful tools for analyzing pearlite [3,4,6,7,15–17]. In the early stages of atom probe development, one-dimensional atom probe (1DAP) has frequently been used to analyze the carbon concentration in deformed pearlitic steels. However, 1DAP is known to probe a very limited number of atoms with a small field-of-view due to a small acceptance angle of the mass spectrometer [28]. In addition, the specimen preparation technique is also crucial for obtaining reliable quantitative atom probe data. Conventional electropolishing methods normally allow for the preparation of cementite lamellae parallel but not normal to the direction of analysis. Thus, the number of detected cementite lamellae is limited by the field-of-view. Furthermore, the spatial resolution in the analysis direction (perpendicular to the lamellar interfaces) is reported to be low [29] due to the local magnification effect [17,30]. These problems can be overcome by applying focused ion-beam (FIB) milling and the lift-out method according to Refs. [31–33]. A substantial number of cementite lamellae, lying perpendicular to the direction of high field-of-view analysis, can be probed with enhanced spatial resolution. Moreover, local electrode atom probe allows us to study the decomposition of cementite more accurately with higher statistical significance as compared to conventional three-dimensional atom probes (3DAP) [3,4,6,7,15–17].

In the present work, a local electrode atom probe (LEAP) is employed to analyze the carbon distribution in three dimensions. The instrument has several advantages over conventional atom probes such as larger probed volumes ($100 \times 100 \times 1000 \text{ nm}^3$) and a higher detection sensitivity due to an improved mass resolution ($\Delta m/m = 1/1100$, full width at half maximum at 27 Da (Da is the atomic mass unit)). Cold-drawn pearlitic steels with true strains ranging from 0 (as-patented) to 5.4 were systematically studied with respect to their carbon distribution. Clear correlations between the carbon concentration in ferrite and the strain as well as between the carbon concentration in the cementite lamellae and their thickness were found. There were also strong indications for the formation of cell/subgrain boundaries in the ferrite and the segregation of carbon atoms at these defects. Based on these findings, the mechanisms of cementite decomposition are discussed in terms of solute–dislocation interactions.

2. Experimental

The materials studied in this work are commercial pearlitic steel wires with eutectoid composition (Fe–0.81C–0.49Mn–0.20Si–0.006P–0.008S wt.% and Fe–3.66C–0.48Mn–0.39Si–0.01P–0.01S at.%) provided by Nippon Steel Corporation. The wires, with an initial diameter of 1.70 mm, were patented with an austenitization treatment at 1223 K for 80 s followed by a pearlitic transformation in a lead bath at 853 K for 20 s. The patented wires were cold-drawn (using lubricants) to true strains ϵ of 0 (as-patented), 0.93, 2, 3.47, 5 and 5.4, respectively.

A LEAP (LEAP 3000X HRTM, Cameca Instruments) was employed to analyze the carbon distribution in three dimensions. The measurements were performed in voltage mode at 70 K under an ultra-high vacuum of 8×10^{-9} Pa. The total voltage during probing was in the range of 6.2–7.2 kV. The pulse fraction was 15%. The pulse repetition rate was 200 kHz at detection rate of 0.005 atom per pulse.

Samples for APT analyses were prepared with the tips perpendicular to the wire axis using a dual-beam FIB (FEI Helios NanoLab 600TM) according to the procedure described in Ref. [29]. Since the friction between the wire and drawing tools can cause more plastic deformation at the surface than in the center of a wire, the microstructure of the wire may be slightly different from the surface to the center. However, this difference decays with increasing drawing strain. For instance, at $\epsilon = 5$, the tips taken from regions 5 and 25 μm below the surface show virtually no difference in terms of the maximum carbon concentration in cementite [29]. To achieve consistent analyses, all tips were taken from the surface regions of the wires. During annular milling about 250 nm of the material was removed from the surface. Thus, the apex of each tip was located about 250 nm below the wire surface.

Samples for TEM observations were prepared with a FIB FEI Nova 600 Nano Lab with electron optics operated at 5 kV, sample preparation done with 30 kV Ga ions, and

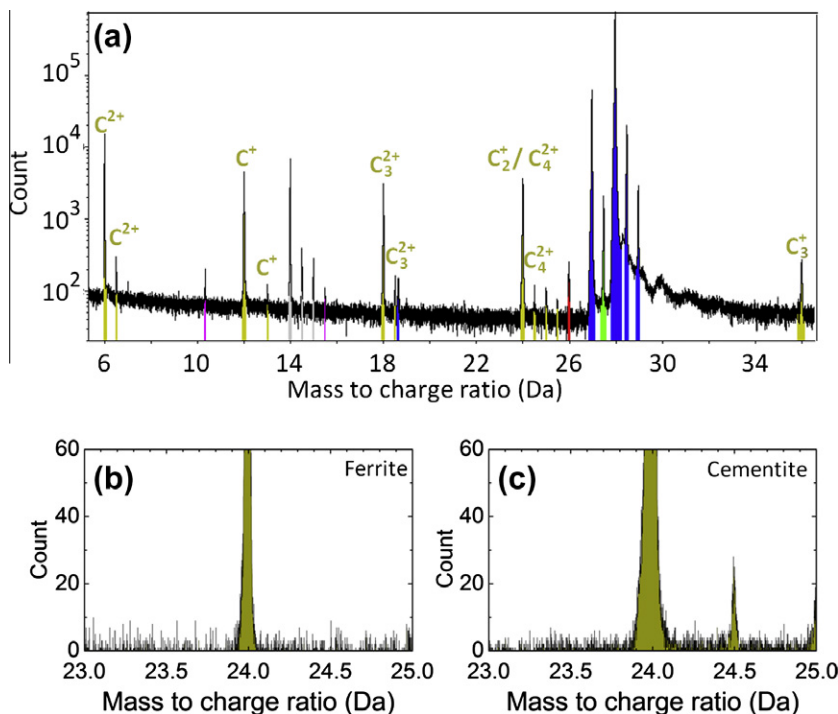


Fig. 1. (a) Example of mass spectrum of a pearlitic steel wire at $\epsilon = 5.4$. All carbon peaks can be identified and are marked. Peaks for the other main elements Fe, Mn and Si are given in blue, green and gray, respectively. (b) and (c) Mass spectra of ferrite and cementite, respectively. Note the presence of the peak of 24.5 Da only in the cementite.

a final finish with 5 kV Ga ions. TEM was performed with a Philips CM30 operated at an acceleration voltage of 300 kV.

3. Results

3.1. Chemical composition measured by using LEAP

Fig. 1 shows a typical mass spectrum of the cold-drawn pearlitic steel wire with $\epsilon = 5.4$. All the mass-to-charge peaks of carbon atoms and molecules are identified and marked. Following a standard assignment method [3,15,29,34,35], the carbon peaks at mass-to-charge ratios $m/n = 6$ and 6.5, 12 and 13, 18 and 18.5, 24.5 and 36 Da can be assigned without ambiguity to C^{2+} , C^+ , C_3^{2+} , C_4^{2+} and C_3^+ , respectively. For the peak at 24 Da, however, there exists an uncertainty; it could be due to either C_2^+ or C_4^{2+} , or a mixture of both. In the literature, this peak is generally assigned as C_2^+ [3,15,29,36].

Taking into account the relative abundance of isotopes of carbon C_4 including mainly $^{12}C_4^{2+}$ and $(^{12}C_3^{13}C)^{2+}$, Sha et al. concluded that over 50% of the ions detected at the peak of 24 Da are in fact C_4^{2+} [35]. Fig. 1a reveals the existence of the isotope $(^{12}C_3^{13}C)^{2+}$ at the peak of 24.5 Da. Thus, there should exist a certain amount of $^{12}C_4^{2+}$ ions at the peak of 24 Da. A further analysis by using a peak decomposition algorithm (supplied by the software IVAS, Cameca Instruments) similar to the calculation method of Sha et al. [35] shows that the contributions of $^{12}C_2^+$ and $^{12}C_4^{2+}$ to this peak are 58% and 42%, respectively. It is

worth noting that the ratios of the two types of ions may differ from one specimen to another, but all values measured in samples with various drawing strains lie in the range of 40–60%.

If the chemical compositions of ferrite¹ (Fig. 1b) and cementite² (Fig. 1c) are separately determined, namely by individually cutting each phase out of the entire volume and evaluating the respective mass spectrum, it is found that the peak of 24.5 Da is only present in cementite but not in ferrite. This means that the peak of 24 Da in ferrite can be exclusively assigned to $^{12}C_2^+$. For cementite, as mentioned above, there must exist a contribution of $^{12}C_4^{2+}$ to the peak of 24 Da. This is confirmed by the quantitative analysis of the peak decomposition algorithm.

Table 1 displays the average chemical compositions (including both ferrite and cementite) measured by LEAP and the nominal values of all samples. The total number of ions detected in each measurement is also given for a statistical evaluation of accuracy. For the peak of 24 Da the C ion is alternatively assigned as $^{12}C_2^+$ and $^{12}C_4^{2+}$. Both results are displayed in Table 1. For the as-patented wire ($\epsilon = 0$) no cementite lamella is detected because of a premature fracture of the sample tip, as the material is relatively soft. Thus, the measured values are obtained only from the ferrite. The measured carbon concentration of 0.05 at.%, which is far above the solubility of carbon atoms in ferrite

¹ Defined here as the region with a carbon concentration lower than 3 at.%.

² The region with a carbon concentration higher than 7 at.%

Table 1
Comparison between the nominal chemical composition and the values measured by LEAP in the case of assigning the peak of 24 Da to C_2^+ and C_4^{2+} . Unit: at.%.

Element	Nominal	$\epsilon = 0$		$\epsilon = 0.93$		$\epsilon = 2.00$		$\epsilon = 3.47$		$\epsilon = 5.00$		$\epsilon = 5.40$	
		C_2^+	C_4^{2+}	C_2^+	C_4^{2+}	C_2^+	C_4^{2+}	C_2^+	C_4^{2+}	C_2^+	C_4^{2+}	C_2^+	C_4^{2+}
C	3.66	0.05	–	2.59	3.19	3.57	4.37	1.98	2.47	2.82	3.55	3.10	3.89
Si	0.39	0.51	–	0.44	0.44	0.43	0.42	0.53	0.53	0.44	0.44	0.48	0.47
Mn	0.48	0.36	–	0.47	0.46	0.47	0.47	0.41	0.41	0.49	0.49	0.23	0.23
Ga	0	0.04	–	0.13	0.13	0.04	0.03	0.31	0.31	0	0	0	0
Total ions		1,980,000		1,300,000		6,800,000		5,100,000		38,000,000		18,900,000	

at equilibrium, indicates that the as-patented state is already in a non-equilibrium condition. This value is in good agreement with that measured in Ref. [15]. The deviation of the measured carbon contents from the nominal values for $\epsilon = 0.93$ and 3.47 is due to premature tip failure and low counting statistics. For larger detected volumes, as in the cases of $\epsilon = 2, 5$ and 5.4, the statistical quality improves. Consequently, the measured average carbon concentrations are in good agreement with the nominal values, in particular, when the weight factors of $^{12}C_2^+$ and $^{12}C_4^{2+}$ at the peak of 24 Da are taken into account. For the elements, which are homogeneously distributed in pearlite, e.g. Si and Mn, the values measured by LEAP are always close to the nominal ones. The results listed in Table 1 are strong indications for a correct measurement of the chemical composition.

3.2. Investigation of lamellar structure of pearlite by TEM and LEAP

Fig. 2 shows the TEM images of pearlitic wires in the as-patented as well as cold-drawn states. The ferrite regions are separated by thin cementite filaments (dark gray). The dark lines, which cross the ferrite and connect two neighboring cementite lamellae (Fig. 2b), mark cell or low-angle grain boundaries of dislocations, as also reported in Ref. [8]. The high strain contrast in the deformed microstructures indicates a high density of deformation-related defects.

In Fig. 2a–c, we observe a refinement of the lamellar structure with increasing drawing strain. The mean ferrite lamella thickness decreases from about 56 nm for the as-patented state to about 10 nm for $\epsilon = 5$. The mean cementite lamella thickness decreases from 17 to 2 nm. This can also be observed in the 3D atom maps of the wires at $\epsilon = 2$ and 5 (Fig. 3). Here, the carbon-enriched (yellow) and -depleted regions (blue) can be identified as cementite and ferrite, respectively. The variation in the lamellar spacing, as for example shown in Fig. 2b, has been consistently reconstructed in the 3D maps (see e.g. Fig. 3 $\epsilon = 2$). Quantitatively, both TEM and APT images indicate that the average interlamellar spacing decreases from an initial value of 70 nm (as-patented) to 25 nm for $\epsilon = 2$ and further to about 13 nm for $\epsilon = 5$. Fig. 4 displays atom maps (top and middle) and the corresponding 1D carbon concentrations profiles (bottom) of the regions taken from Fig. 3.

Clearly, in addition to the refinement of lamellar spacing, the cementite filaments also become thinner, while the phase boundaries become blurred.

3.3. Carbon concentration in ferrite and cementite

One-dimensional concentration profiles have been frequently used to quantify the overall carbon concentration in pearlitic steel wires [3,4,15,29]. As Fig. 4 shows, when the drawing strain increases from 2 to 5, the carbon concentration in cementite decreases to about 10 at.%, far below the stoichiometric value of 25 at.%. Concomitantly, the carbon concentration in ferrite rises up to 2 at.%. Both findings give direct evidence of cementite decomposition. While the tendency of changing carbon concentrations in both phases is correct, the extraordinarily high carbon concentration of 2 at.% in ferrite is discussed in the following. As mentioned above, for ferrite the peak of 24 Da exclusively corresponds to $^{12}C_2^+$. For cementite, $^{12}C_4^{2+}$ should also be taken into account. Thus the carbon atoms in ferrite and cementite cannot be correctly assigned with an overall 1D concentration profile consisting of both phases. Instead, as proposed in our previous work [37], to achieve a better accuracy in the analysis, one should isolate each phase from the entire 3D volume separately and perform an individual analysis. The details of the subcutting method are reported in Ref. [37].

Fig. 5 shows the carbon concentrations (measured with the subcutting method) in ferrite as a function of wire strain. Each data point is obtained from averaging over 3–10 measurements. The values measured in all wires lie below 0.6 at.% C, which is much smaller than the value obtained from the 1D concentration profiles (Fig. 4). It is seen that the solubility of carbon atoms in ferrite is not a monotonically increasing function of the drawing strain, but starts to saturate at a certain strain ($\epsilon \geq 3.47$ in the present work). This observation implies that a saturation of cementite decomposition may also occur at that strain.

The data found in the literature [13,37] (dash-dotted line with small open square symbols) shows a similar concentration–strain relation but with a higher carbon saturation concentration. The higher saturation concentration can be attributed to the fact that this material contains a higher overall carbon concentration of 4.40 at.% than the present material (3.66 at.%).

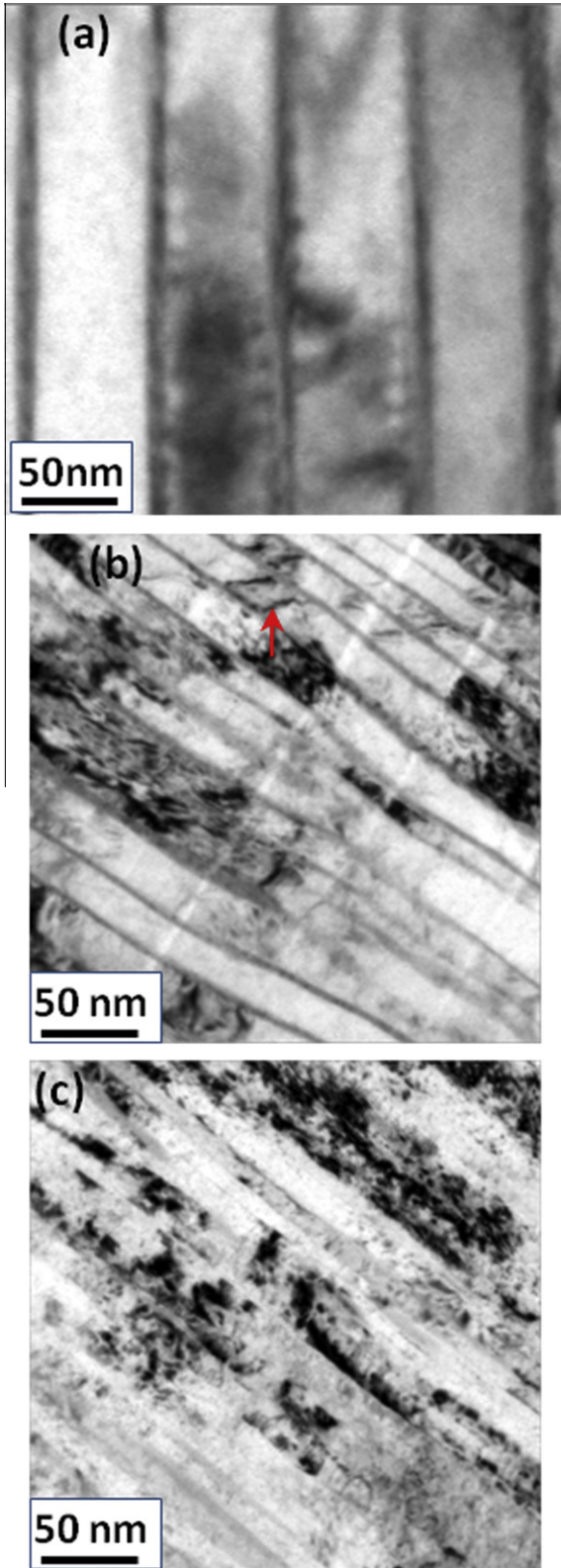


Fig. 2. TEM images of wires taken in longitudinal direction for (a) as-patented state, (b) $\epsilon = 2$ and (c) $\epsilon = 5$. The arrow marks one of the cell boundaries.

Fig. 6 displays the carbon concentration in cementite as a function of the lamellar thickness. The carbon concentra-

tion is measured in the middle of each cementite lamella to avoid errors due to variations in the local magnification (the so-called local magnification effect, see [37] for more details). All samples of different strain share a common feature: the carbon concentration decreases with decreasing thickness of the cementite lamellae. For the same cementite thickness the carbon concentration decreases during further straining from $\epsilon = 2$ –3.47. It should be noted that the influence of strain is inverse to the thickness. The curves show a tendency that in those cementite lamellae with sufficient thickness the strain effect may become negligible and the carbon concentration matches the stoichiometric value of 25 at.% for Fe_3C . For $\epsilon \geq 3.47$ the influence of the drawing strain disappears so that the cementite filaments with the same thickness exhibit the same carbon concentration. This is consistent with the results observed in Fig. 5 where the carbon concentration in ferrite saturates at the same strain.

Evidently, as shown in Figs. 5 and 6, the decomposition is promoted by plastic deformation but within a limited strain regime. Above a critical strain, e.g. 3.47 in the present case, the decomposition of cementite does not proceed. This means that the effect of plastic deformation on cementite decomposition has its limit. In fact, a lamellar structure still exists in the wire produced at even higher plastic deformation of $\epsilon = 6.02$ [37]. The saturation of cementite decomposition at high strain has also been confirmed by Mössbauer spectroscopy investigations [20,38].

The transport of carbon atoms from cementite into ferrite should, in principle, follow the rule of mass balance, namely the loss of carbon atoms in cementite is compensated by the same amount of atoms in ferrite. This leads to a direct connection between the changes of carbon concentration in both phases. According to the carbon concentration in cementite shown in Fig. 6, we are able to estimate the corresponding carbon concentration in ferrite on the basis of the rule of mass balance (see Appendix A for the detailed estimation procedure). The calculation yields a concentration in ferrite of 0.55 at.% C for $\epsilon = 2$ and 1.46 at.% C for $\epsilon \geq 3.47$, which are distinctly larger than the respective measured values of 0.3 and 0.5 at.% C (see Fig. 5). However, it should be noted that the data shown in Fig. 5 are measured only in the selected regions (relatively far from the cementite) with a concentration of less than 3 at.% C. If the regions of a carbon concentration between 3 and 7 at.%, which are located near the phase boundaries, are also considered as ferrite, the average carbon concentration in ferrite would increase up to 0.5 at.% for $\epsilon = 2$ and 1.3 ~ 1.7 at.% for $\epsilon \geq 3.47$, respectively, which are in good agreement with the estimated values, as shown in Fig. 7. While these regions dramatically enhance the average carbon concentration in ferrite, they hold volume fractions of only 5% for $\epsilon = 2$ and 15% for $\epsilon \geq 3.47$, respectively. This would mean a strongly heterogeneous distribution of carbon atoms in ferrite so that most carbon atoms are located near the phase boundary, where most of dislocations get stored.

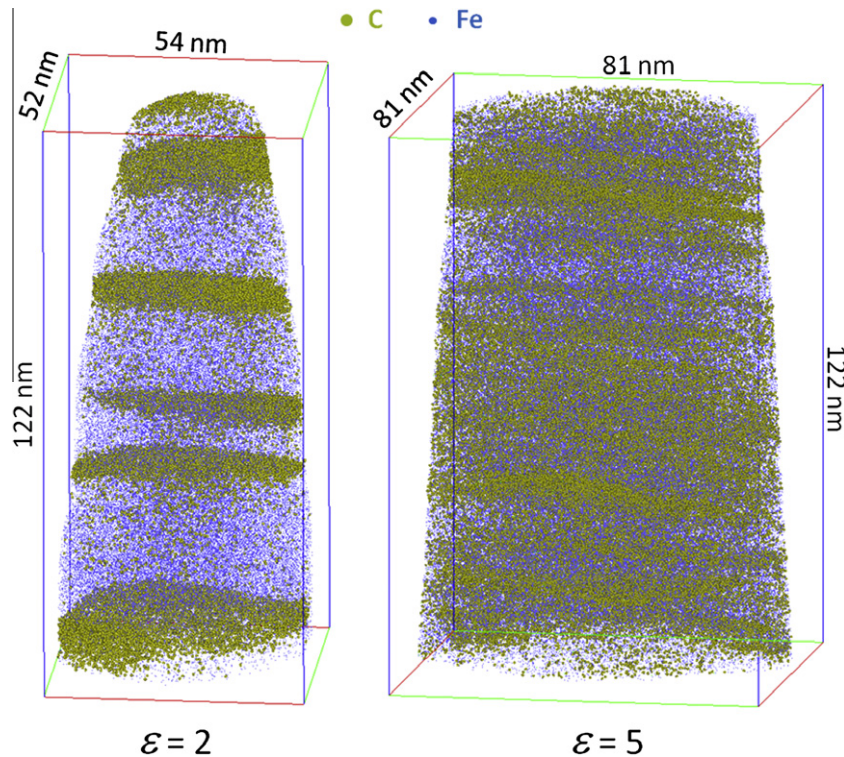


Fig. 3. 3D atom maps of cold-drawn wires for $\epsilon = 2$ (left) containing roughly 6.8×10^6 atoms within a volume of $54 \times 52 \times 122 \text{ nm}^3$ and $\epsilon = 5$ (right) containing 16.2×10^6 atoms within a volume of $81 \times 81 \times 122 \text{ nm}^3$. For clarity only 2% of the iron (blue) and 20% of the carbon (yellow) atoms are displayed.

3.4. Segregation of carbon atoms in ferrite

Fig. 8a shows a 3D map of carbon atoms for a wire at $\epsilon = 0.93$. A region of interest (ROI) (marked by the pink box) is selected from the ferrite for a closer investigation. As can be seen from Fig. 8b, the distribution of carbon atoms is not homogeneous. The carbon atoms are mainly located in a curved region, while the rest of the selected ROI is virtually free of carbon atoms. Fig. 8c displays the 3D map for Si and Mn atoms in the ROI, where both elements are distributed relatively homogeneously. The latter observation has been reported previously [3,29]. This result is also confirmed by the nearest-neighbor distance distributions for Si and Mn atoms (Fig. 8e). For carbon atoms, as shown in Fig. 8d, the measured data (solid line) deviates from the randomized distribution (dotted line), indicating their inhomogeneous distribution in the ROI.

Fig. 9 shows another sample observed in the wire produced with $\epsilon = 2$. One can recognize two carbon-enriched zones in the ferrite (marked B1 and B2), which reach from one cementite lamella to the neighboring one (see top figure). The 3D carbon atom map of the ROI shown in Fig. 10 (front view) highlights a strip intersecting with zone B2 at the top of Fig. 9. We interpret the carbon enrichment in the two-dimensional zones B1 and B2 as cell or low-angle grain boundaries, as confirmed by TEM observations [8,14]. Most carbon atoms are segregated at the boundary (see Fig. 10a and c). In contrast, Mn and Si atoms are

homogeneously distributed throughout the cell, as shown in Fig. 10b and d.

The segregation of carbon atoms at grain boundaries is more frequently observed in the materials drawn to even higher strains of 3.47 and 5.4. For example, Fig. 11 shows that, in a small selected volume, two parallel cell/low-angle grain boundaries exist. The 2D boundary surface is also revealed by the closer investigation of the ROI (marked with pink color) as shown in Fig. 11b and c. The segregation of carbon atoms at the boundary can be easily recognized from both the atom maps shown in Fig. 11b and c and the concentration profile in Fig. 11d. It should be noted that the peak carbon concentration located in the center of the boundary is higher by a factor of about 2 than that found in Fig. 10c. This observation is a strong indication that cementite decomposition and carbon segregation to cell or grain boundaries are both promoted by plastic deformation. The distribution of Si and Mn atoms is also shown in the figure to validate the statistics for the measurement. Both elements are homogeneously distributed in the sample as also seen in Fig. 10d.

4. Discussion

SPD is an efficient method of refining the lamellar structure of pearlite, and involves refining the thickness as well as the spacing of the cementite lamellae. Such a refinement can be observed by scanning electron microscopy (SEM) [39] and TEM [2]. The refinement of the cementite lamellae

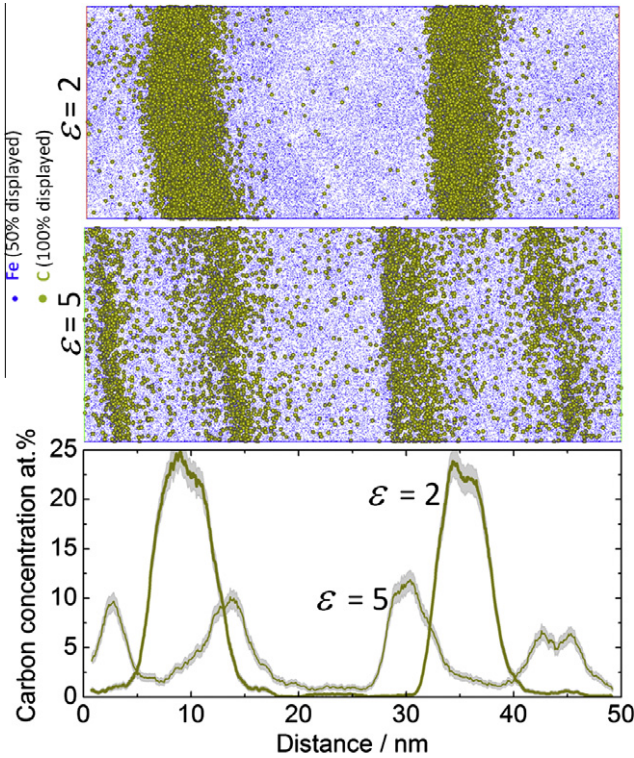


Fig. 4. Atom maps of the selected volume of $4 \times 20 \times 50 \text{ nm}^3$ in the cold-drawn pearlitic wires at $\epsilon = 2$ (upper) and $\epsilon = 5$ (middle). The large yellow dots and the small blue dots represent carbon (100% shown) and iron (50% shown), respectively. The bottom figure shows the corresponding 1D carbon concentration profiles along the direction perpendicular to the lamellar interfaces (also the probing direction). The error bars are marked in gray.

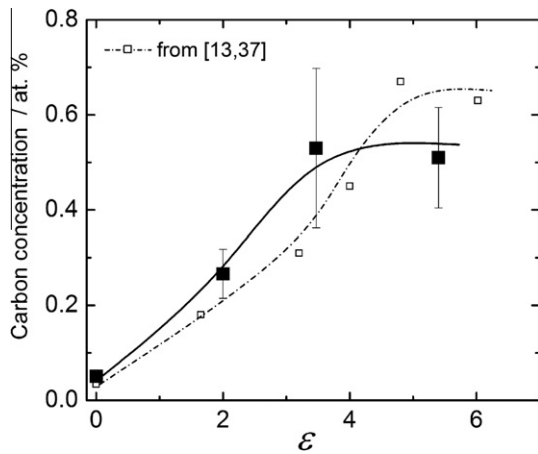


Fig. 5. Carbon concentrations in ferrite as a function of wire strain. Literature data are taken from Ref. [13,37].

is partly due to the plastic deformation occurring inside the cementite phase [2], and partly due to chemical decomposition as described in Section 3. In Section 3.4 we found cell/low-angle grain boundaries in ferrite at which the dissolved carbon atoms are segregated. We first discuss the possibility of the formation of cell/grain structures in ferrite.

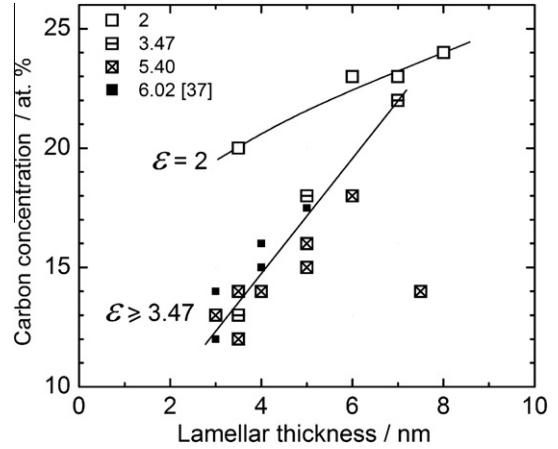


Fig. 6. Carbon concentrations in the cementite as a function of lamella thickness.

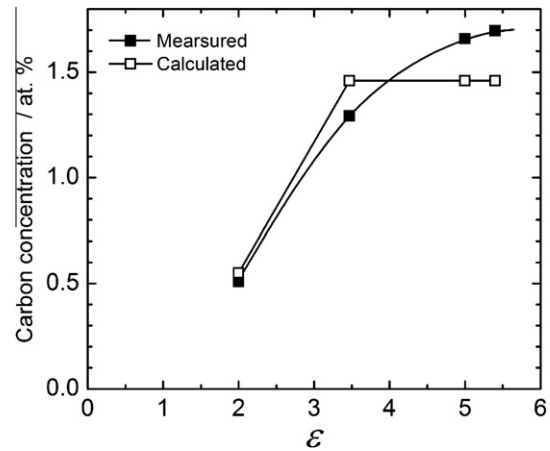


Fig. 7. Comparison of the estimated carbon concentrations with that measured in the regions with a carbon concentration lower than 7 at.%. The measurement errors are within $\pm 0.03\%$.

4.1. Evolution of dislocation structure in ferrite

The dislocation densities measured for the pearlite wire by using X-ray line profile analysis vary from a minimum value of $\rho = 7.8 \times 10^{14} \text{ m}^{-2}$ at $\epsilon = 0$ (as-patented) to a maximum value of $1.4 \times 10^{16} \text{ m}^{-2}$ at $\epsilon = 5$ [40]. These values correspond to an average dislocation spacing $\rho^{-0.5}$ of ~ 35 and ~ 8 nm, respectively. The mean free path of dislocations is proportional to the average dislocation spacing. For a safe estimate, if we take the proportionality constant as 10, the mean free paths turn out to be ~ 350 and ~ 80 nm, which are larger than the interlamellar spacings of ~ 60 and ~ 20 nm in each material, respectively. A similar estimate was also made by Gil Sevillano that the thickness of the ferrite lamellae are approximately 50 times lower than the mean free path of dislocations and less than 10 times the mean interdislocation distance that would develop under free gliding conditions [41]. This means that the formation of a dislocation structures in the ferrite channel, such as a cell or subgrain, is not likely because the probability of dislocation interaction is low.

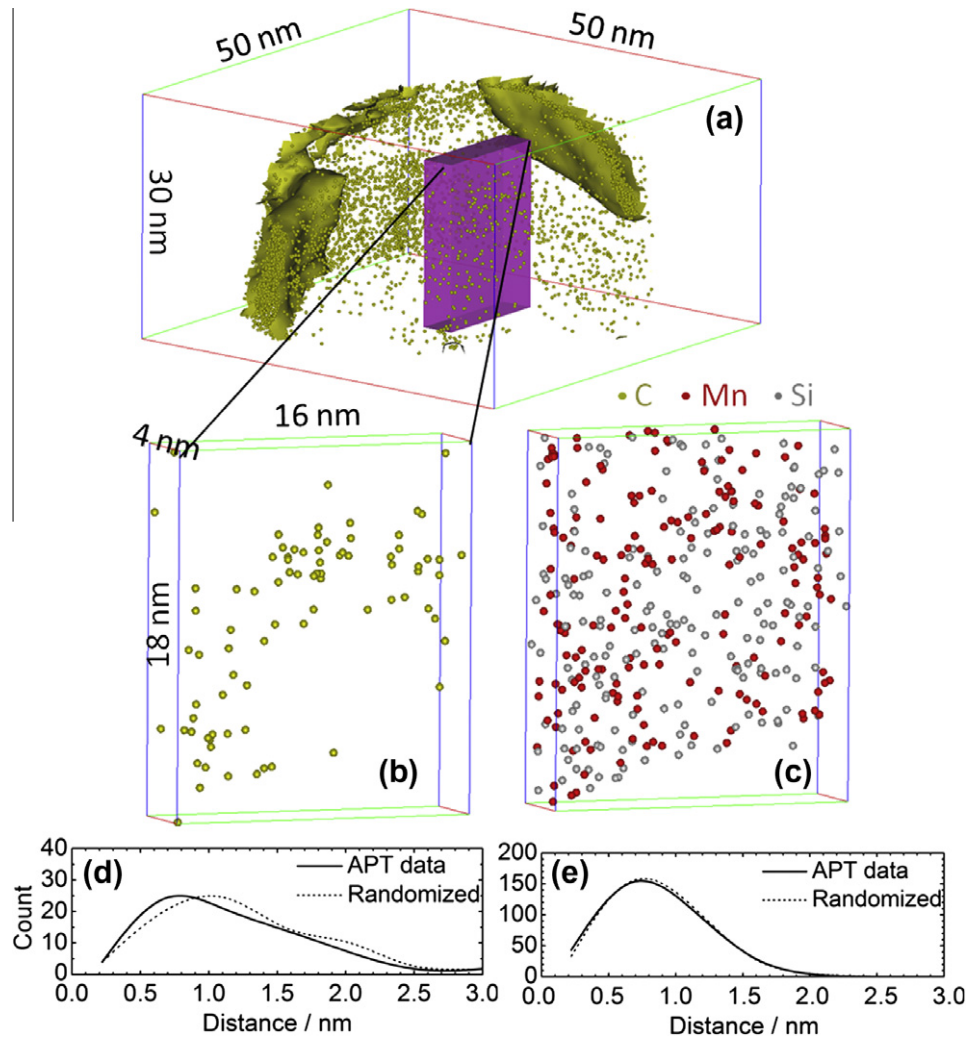


Fig. 8. (a) 3D map of carbon atoms with an isoconcentration surface drawn at 7 at.% C for the pearlitic steel wire at $\epsilon = 0.93$. Only 50% of carbon atoms are displayed. (b) The distribution of C in the ROI taken from (a). 100% of the detected carbon atoms are displayed. (c) Analogue of (b) for Mn (red) and Si (gray). The blank area at the bottom is due to lack of material at the specimen tip. (d) Nearest-neighbor distance distributions between the carbon atoms. (e) As (d) for Mn and Si atoms.

Let us consider this problem in 3D space (Fig. 12). Similar to the schematics shown in Ref. [42], consider a general case that the slip plane of dislocations is inclined to the drawing direction and also to the normal direction of the cementite lamellae. At the interface between ferrite and cementite, dislocations can be nucleated provided that there is a mismatch in the elastic moduli of the two phases, and provided that some heterogeneities are present along the interface, which act as stress concentrators [43]. Regarding the dislocation sources, here we consider two possible mechanisms of dislocation multiplication for pearlite with narrow interlamellar spacings as shown in Fig. 12. In contrast to the Frank–Read source, which consists of two pinned ends (see Fig. 12a), the bulging mechanism does not involve any fixed source size. Instead, dislocations bulge out into the ferrite from lamellar interfaces [43] (see Fig. 12b). Gil Sevillano [41] proposed interfacial and intraphase dislocation sources, where dislocations glide between two impenetrable interfaces and within the interlamellar channels, respectively. Such

types of dislocation sources may dominate for the pearlite with coarse interlamellar spacings, because the critical stress for the corresponding configuration is low, and therefore preferable.

Since the mean free path of dislocations is larger than the lamellar spacing, the dislocation segment which reaches the opposite cementite plate must get stored there (see the cementite plate on the top). A further movement of the dislocation segments (corresponding to a further expansion of the dislocation loop) is only possible when the Orowan stress due to the line tension of the dislocation is overcome. The Orowan stress is inversely proportional to the interlamellar spacing. When the interlamellar spacing is sufficiently small, the Orowan stress can be so high that a further movement becomes difficult and the free dislocation segments will get stored in the ferrite.

Associated with the dislocation bulging, when the free segments tend to extend out of the narrow channel, a high Orowan stress has to also be reached, which leads to the storage of free dislocation segments in the ferrite. There-

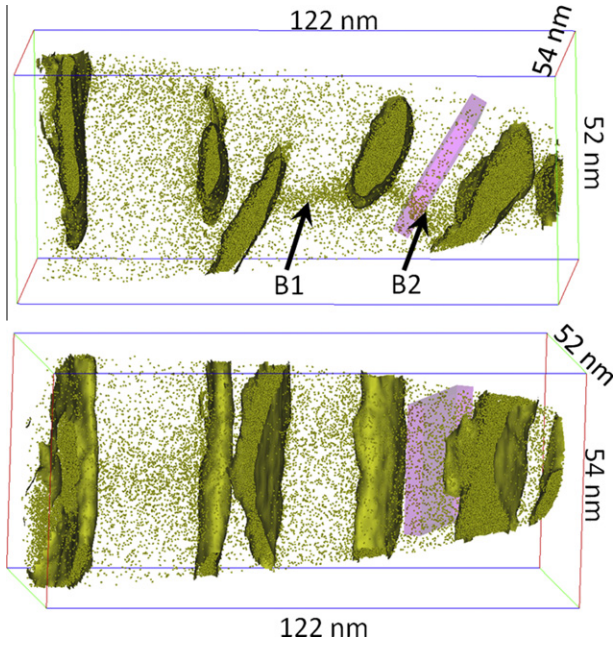


Fig. 9. 3D carbon atom maps with an isoconcentration surface drawn at 7 at.% Carbon for the pearlitic wire at $\epsilon = 2$. Top and bottom images show two side views (rotated 90° with respect to each other) of cementite lamellae, respectively. Only 50% of carbon atoms are displayed. The two grain boundaries B1 and B2 with carbon segregation are marked by the arrows. The detailed 3D map of the region of interest (pink box) with a volume of $30 \times 30 \times 4 \text{ nm}^3$ is shown in Fig. 10.

fore, in either case, dislocations will deposit not only at the interface but also inside the ferrite. When dislocations nucleated from parallel slip planes, a dislocation wall can be formed along the longitudinal direction of the lamellae.

Consider that dislocations with the same Burgers vector but opposite sign can be nucleated from opposite interfaces, the dislocation wall may also contain dislocations of different sign. Thus the wall could be a cell boundary or a grain boundary depending on the net sign of the dislocations involved. This mechanism can explain the formation of cell/subgrain boundaries, such as at positions B1 and B2 as shown in Fig. 9.

4.2. Segregation of carbon atoms at the lattice defects in ferrite

Based on literature data, Gavriljuk [22] excluded the possibility of formation of solid solution when cementite decomposes. Instead, he suggested that the dissolved carbon atoms are mainly located at the dislocations that are stored at the ferrite–cementite interface. The dislocation mechanism discussed above supports this analysis. However, we further suggested that dislocation walls can be formed inside ferrite and we assume that the dissolved carbon atoms can also be segregated to these new interfaces. This suggestion is supported by the 3D carbon atom map shown in Figs. 10 and 11. These results are consistent with the fact that the binding energy between dislocations and carbon atoms is higher than that between carbon atoms and iron in cementite [24–26]. Therefore, the distribution of carbon atoms is closely related to the distribution of dislocations. As discussed above, a heterogeneous dislocation structure forms in the ferrite lamellae, which consequently leads to an inhomogeneous distribution also of carbon in the ferrite.

Recently, Kobayashi et al. [44] reported an anomalous distribution of carbon atoms in ferrite of heat-treated

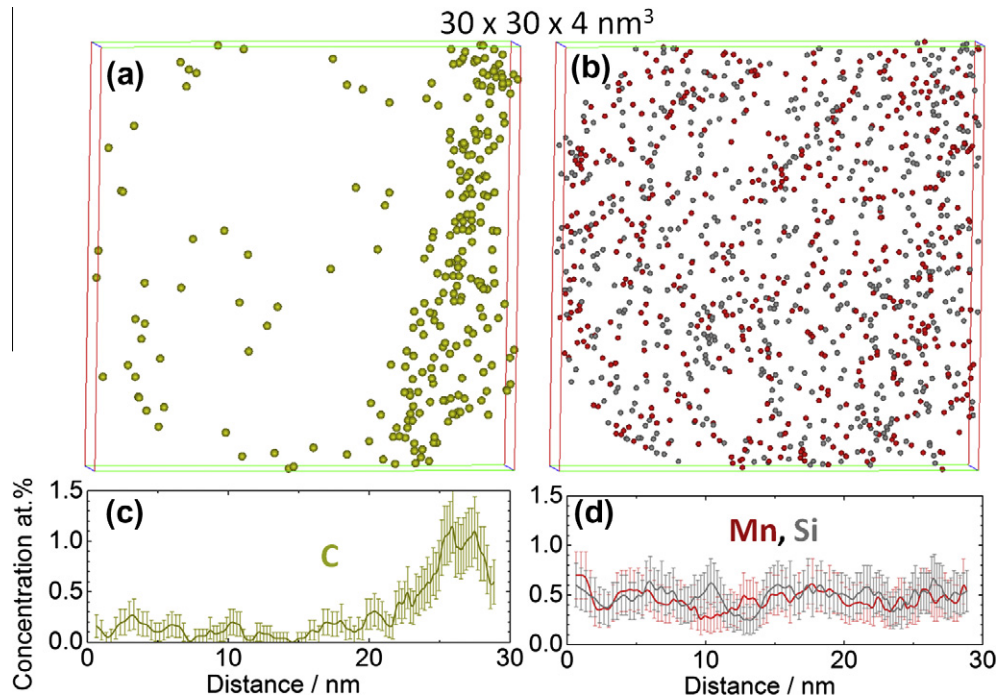


Fig. 10. Distribution of carbon atoms (a) as well as Mn (red) and Si (gray) atoms (b) in the ROI taken from Fig. 9 (ferrite region). All atoms detected are displayed. (c) and (d) show the corresponding 1D concentration profiles for carbon and Si and Mn, respectively.

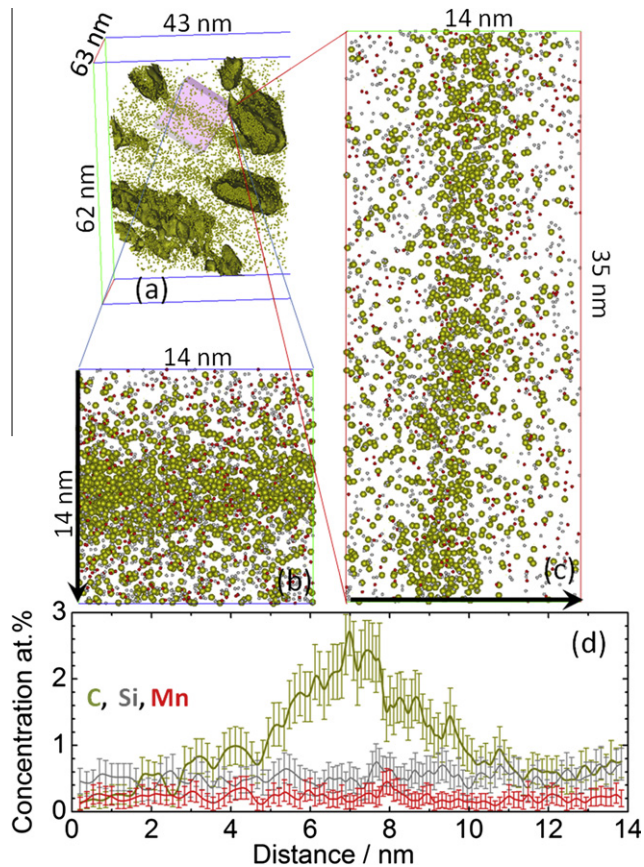


Fig. 11. (a) Part of the 3D carbon atom map with an isoconcentration surface at 7 at.% C for wires at $\epsilon = 5.4$. (b) and (c) Front and side views, respectively, of the atom maps for the ROI taken from (a). The yellow, red and gray dots represent C, Mn and Si atoms, respectively. (d) 1D concentration profiles for the three elements shown in (b) and (c) (fixed count of 5000 atoms) along the direction (marked with the black arrows) perpendicular to the carbon-enriched boundary.

(773 K for 5 h) pearlitic wire, where carbon atoms were always enriched in certain crystallographic directions [44]. They attribute this enrichment to the difference of the trajectory between iron and solute carbon atoms during their flight in the APT measurement. However, similar observations could not be made in the present investigations. Recent LEAP analyses done in our group on cold-drawn wires annealed at 400 °C for 0.5 h clearly showed that carbon atoms are preferentially located at the boundaries of hexagonal (sub) grains in the ferrite. This means that the detected carbon segregation in this work reflects a real physical process.

It is known that the cell or grain size is dependent on the stress and the strain (before a steady state of deformation is reached under given deformation conditions). Thus, further wire drawing leads to additional work hardening, which causes a finer dislocation structure. In other words, the more cell or grain boundaries are formed upon further straining, the more segregation of carbon atoms in the ferrite is possible. This may explain the fact that the carbon concentration in ferrite increases with drawing strain (see Fig. 5). Following this line of argument, the saturation of

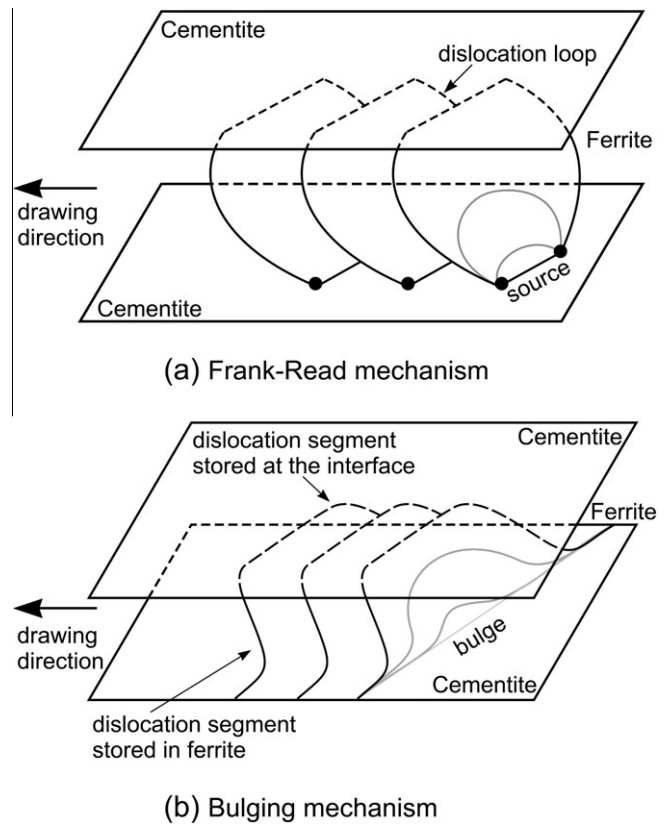


Fig. 12. Schematic diagram explaining the formation of dislocation cell structures in the ferrite modified after Ref. [42]. The slip plane of the dislocations is inclined to the cementite lamellae and the drawing direction. Dislocations may be emitted from Frank–Read sources (a) and according to a bulge mechanism [43] (b).

carbon atoms at higher strains should be coupled to the saturation in the dislocation density that can be stored in the ferrite. In the recent measurements of the dislocation density performed with X-ray line profile analysis for the same materials, it was indeed found that the increase of the dislocation density with strain becomes significantly slower at high strains ($\epsilon \approx 4$) [40].

4.3. Thermodynamics and kinetic mechanisms of cementite decomposition

There are two principal interpretations for cementite decomposition in the literature. Based on our results and those found in the literature, we consider that the interaction between carbon atoms and dislocations is likely to be the mechanism responsible for cementite decomposition. Let us start with reviewing the available findings. First, cold working introduces a high density of dislocations at the interfaces between ferrite and cementite [43,45]. Second, the interaction between dislocations and carbon atoms exhibits a higher binding energy [24] than that between carbons and iron atoms in cementite [25,26]. Third, carbon atoms segregate at cell/grain boundaries in ferrite [46] (see also Section 3 above). Fourth, the saturation of the carbon

concentration in the ferrite with strain is associated with a slow increase of the dislocation density at high strains.

These results suggest that the dislocation activity and cementite decomposition are associated phenomena and occur simultaneously during plastic deformation. When the dislocation loops expand from one interface to the opposite one, they also drag the carbon atoms out of the cementite lattice and form a Cottrell atmosphere during motion. The dislocations in ferrite form dislocation walls, which connect the neighboring cementite plates as shown in Figs. 10 and 11 and are decorated with an enhanced amount of carbon atoms.

According to this mechanism, the degree of cementite decomposition is determined by the dislocation structure and its evolution, which in turn is controlled by the drawing stress and strain. A higher degree of plastic deformation introduces a higher density of dislocations which form more cell/grain boundaries. As a result, cementite decomposition is more severe. This leads to a thinning of cementite plate with a reduced carbon concentration (see Fig. 6) and an enhancement of the average carbon concentration in ferrite (see Fig. 5). Gradual saturation in the dislocation structure leads to the saturation in the interaction between dislocations and cementite lamellae. Thus, the relation between the carbon concentration and the thickness of cementite lamellae becomes strain independent (see Fig. 6). For the cementite lamellae with a thickness larger than ~ 8 nm, as shown in Fig. 6, dislocations may not be able to approach the center of the lamellae even after the highest drawing strain. This means that carbon atoms inside the cementite cannot reach the ferrite dislocations, while carbon near the interfaces can leave the cementite and be stored at the dislocations in the ferrite. Thus, the influence of the neighboring ferrite dislocations saturates upon further deformation, as the dislocation density in the ferrite saturates.

In addition to the elementary interaction between carbon atoms and lattice dislocations in the ferrite, a trans-phase dislocation-shuffle mechanism may act as a kinetic mechanism for the decomposition of cementite [47,48]. According to the mechanism discussed in Ref. [47], provided that dislocations penetrate from ferrite into cementite on more than one active slip system, the shearing of atomic planes along mutually inclined directions can create interface steps and embed small cementite particles in ferrite. Such tiny cementite particles can be further cut by dislocations gliding through them, which enhances the energy of the particles through the Gibbs–Thomson effect so that they finally dissolve. In principle, this mechanism can explain the large deformation-driven transport of carbon from cementite into the ferrite against the thermodynamic equilibrium conditions. However, the effect of this mechanism may be conditioned by several factors, e.g. the magnitude of the resolved shear stress of the dislocations approaching the interface on the activated system, the degree of misorientation between the active slip planes on either side of the interface and the energetic preferability

of the resulted configuration which can, for example, be influenced by the residual dislocation content at the interface through the selection of a transmitted slip system in the body-centered cubic phase [49]. Misra et al. suggested that transmission of dislocations across interfaces is only likely to occur at nanometer length scales (e.g., ~ 1 – 2 nm layer thickness) [50]. The observed broken cementite lamella in pearlite [51] may be an indicator of penetration of ferrite dislocations through the thin cementite lamella [48].

5. Conclusions

Cementite decomposition and the associated mechanical alloying in cold-drawn pearlitic steel wires was studied as a function of true drawing strain by using LEAP in conjunction with TEM. The carbon concentrations in ferrite, cementite, and the entire analyzed volumes were measured systematically by applying a decomposition algorithm for overlapping mass-to-charge peaks of carbon. Cementite decomposition was found to be promoted by plastic deformation. However, the decomposition of cementite and the carbon concentration in ferrite both saturate after a true drawing strain of 3.47, and thus the lamellar structure exists even at a drawing strain of up to 5.4. Strong indications for the formation of cell-grain boundaries in ferrite, at which most of carbon atoms in ferrite segregate, were observed. Based on these findings, we suggest that the dislocation density in the ferrite is probably the mechanism underlying cementite decomposition.

Acknowledgments

The authors thank Dr. S. Nishida from Nippon Steel Corporation for providing the cold-drawn specimens, and Drs. D. Ponge from Max-Planck Institut für Eisenforschung and Y.Z. Chen from Georg-August-Universität Göttingen for valuable discussions. We are grateful to the Deutsche Forschungsgemeinschaft for funding this research (Project SFB 602).

Appendix A. Simple estimate of the carbon balance after cementite decomposition

A.1. C-concentration in the cementite

Each cementite lamella is cut by the same number of dislocations per area A which removes a total of n mol C per area from the carbide. Then the C-concentration changes from 0.25 to x according to the following balance:

$$x \frac{Ad}{\Omega_C} = 0.25 \frac{Ad}{\Omega_C} - \Delta nA \quad (1)$$

where d is the thickness of the lamella and Ω_C the molar volume of cementite. Rearranging yields:

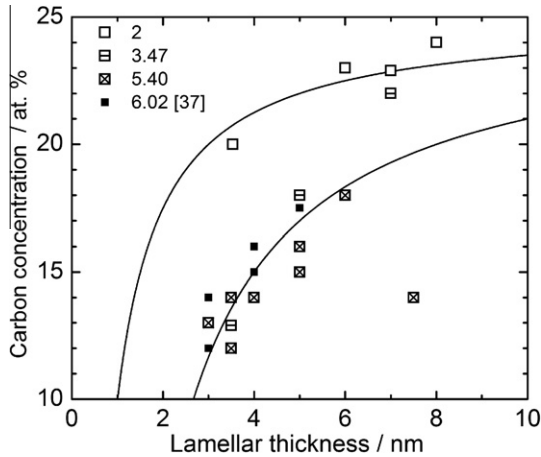


Fig. A.1. C-concentration in cementite x after deformation as a function of the lamella thickness d . Lines are fit to Eq. (2).

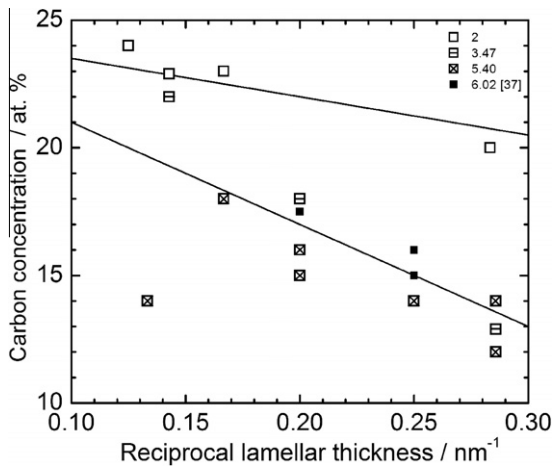


Fig. A.2. C-concentration vs. d^{-1} according to Eq. (2).

$$x = 0.25 - \Delta n \frac{\Omega_C}{d} \quad (2)$$

As shown in Fig. A.1, this equation agrees well with the experimental data. The process of C-removal stops at large strains, when the dislocations are entering the cementite from the ferrite with the same amount of carbon as they take out when they leave the cementite to enter the ferrite.

A.2. C-concentration in the ferrite

In ferrite, the released carbon Δn_{tot} per area A for a number of lamellae, Z , is given by:

$$A\Delta n_{\text{tot}} = Z\Delta nA \quad (3)$$

Z is obtained from the total volume of cementite divided by the average volume of one lamella:

$$Z = \frac{V_{\text{Cem}}}{Ad_{\text{aver}}} = \frac{x_w V_w}{25Ad_{\text{aver}}} = \frac{x_w Ad_w}{25Ad_{\text{aver}}} = \frac{x_w d_w}{25d_{\text{aver}}} \quad (4)$$

where d_{aver} is the average thickness of cementite lamella and x_w and d_w are the C-concentration and thickness of the wire:

$$\Delta n_{\text{tot}} = \Delta n \frac{x_w d_w}{25d_{\text{aver}}} \quad (5)$$

This will change the C-concentration in the ferrite to:

$$\Delta C_{\text{fer}} = \frac{\Delta n_{\text{tot}} A \Omega_{\text{fer}}}{Ad_w} = \Delta n \frac{x_w \Omega_{\text{fer}}}{25d_{\text{aver}}} = \frac{\text{slope} x_w \Omega_{\text{fer}}}{\Omega_C 25d_{\text{aver}}} \quad (6)$$

where slope is the slope of the concentration vs. d^{-1} plot, x_w is the total C-concentration of the wire in at.% and Ω_{fer} is the atomic volume of ferrite. Using $\Omega_C = \Omega_{\text{fer}}$, slope = 40 at.% nm (from Fig. A.2 for larger strains) $d_{\text{aver}} = 4$ nm and $x_w = 3.66$ at.% yields $\Delta C_{\text{fer}} = 1.46$ at.% C. For $\epsilon = 2$ the slope is 15 at.% nm (from Fig. A.2 for lower strain), yielding $\Delta C_{\text{fer}} = 0.55$ at.% C.

References

- [1] Takahashi T, Ochiai I, Tashiro H, Ohashi S, Nishida S, Tarui T. Nippon Steel Tech Rep 1995;64:45.
- [2] Landford G. Metall Trans A 1977;8:861.
- [3] Hong MH, Reynolds Jr WT, Tarui T, Hono K. Metall Mater Trans A 1999;30:717.
- [4] Hono K, Ohnuma M, Murayama M, Nishida S, Yoshie A. Scripta Mater 2001;44:977.
- [5] Taniyama A, Takayama T, Arai M, Hamada T. Scripta Mater 2004;51:53.
- [6] Goto S, Kirchheim R, Al-Kassab T, Borchers C. Trans Nonferrous Met Soc China 2007;17:1129.
- [7] Borchers C, Al-Kassab T, Goto S, Kirchheim R. Mater Sci Eng A 2009;502:131.
- [8] Embury JD, Fisher RM. Acta Metall 1966;14:147.
- [9] Gridnev VN, Gavriljuk VG, Dekhtyar IY, Meshkov YY, Nizin PS, Prokopenko VG. Phys Status Solidi A 1972;14:689.
- [10] Read HG, Reynolds Jr WT, Hono K, Tarui T. Scripta Mater 1997;37:1221.
- [11] Tarui T, Takahashi T, Ohashi S, Uemori R. Iron Steelmaker 1994;21:25.
- [12] Tarui T, Takahashi J, Tashiro H, Nishida S. In: Paris HG, Kim DK, editors. Processing and applications of metal wires. Warrendale, PA: TMS; 1996. p. 87.
- [13] Maruyama N, Tarui T, Tashiro H. Scripta Mater 2002;46:599.
- [14] Tarui T, Maruyama N, Takahashi J, Nishida S, Tashiro H. Nippon Steel Tech Rep 2005;91.
- [15] Danoix F, Julien D, Sauvage X, Copreaux J. Mater Sci Eng A 1998;250:8.
- [16] Sauvage X, Copreaux J, Danoix F, Blavette D. Philos Mag A 2000;80:781.
- [17] Sauvage S, Lefebvre W, Genevois C, Ohsaki S, Hono K. Scripta Mater 2009;60:1056.
- [18] Yamada Y. Trans ISIJ 1976;16:417.
- [19] Gridnev VN, Nemoshkalenko VV, Meshkov YY, Gavriljuk VG, Prokopenko G, Razumov ON. Phys Status Solidi A 1975;31:201.
- [20] Nam WJ, Bae CM, Oh SJ, Kwon SJ. Scripta Mater 2000;42:457.
- [21] Belous MV, Cherepin VT. Fiz Metall Metalloved 1961;12:685.
- [22] Gavriljuk VG. Scripta Mater 2001;45:1469.
- [23] Gavriljuk VG. Mater Sci Eng A 2003;345:81.
- [24] Cocharadt AW, Schoek G, Wiedersich H. Acta Metall 1955;3:533.
- [25] Johnson RA, Diens GI, Damask AC. Acta Metall 1964;12:125.
- [26] Johnson RA. Acta Metall 1967;15:513.
- [27] Languillaume J, Kapelski G, Baudet B. Acta Mater 1997;45:1201.
- [28] Kelly TF, Miller MK. Rev Sci Instrum 2007;78:031101.
- [29] Takahashi J, Tarui T, Kawakami K. Ultramicroscopy 2009;109:193.
- [30] Sauvage X, Thilly L, Blavette D. J Phys IV France 2001;11:27.
- [31] Miller MK, Russell KF, Thompson GB. Ultramicroscopy 2005;102:287.

- [32] Miller MK, Russell KF, Thompson K, Alvis R, Larson DJ. *Microsc Microanal* 2007;13:428.
- [33] Thompson K, Lawrence D, Larson DJ, Olson JD, Kelly TF, Gorman B. *Ultramicroscopy* 2007;107:131.
- [34] Takahashi J, Kawakami K, Yamaguchi Y. *Microsc Microanal* 2009;15(Suppl 2):3036.
- [35] Sha W, Chang L, Smith GDW, Cheng L, Mittemeijer EJ. *Surf Sci* 1992;266:416.
- [36] Miller MK, Beaven PA, Brenner SS, Smith GDW. *Metall Trans A* 1983;14:1021.
- [37] Li YJ, Choi P, Borchers C, Chen YZ, Goto S, Raabe D, et al. *Ultramicroscopy* 2011. doi:10.1016/j.ultramic.2010.11.010.
- [38] Gavriljuk VG. Carbon distribution in steel (in Russian). Kiev: Naukova dumka; 1987.
- [39] Zelin M. *Acta Mater* 2002;50:4431.
- [40] Chen YZ, Csiszár G, Cizek J, Westerkamp S, Borchers C, Ungr T, et al. Unpublished results; 2010.
- [41] Gil Sevillano J. *J Phys III* 1991;1:967–88.
- [42] Schastlivtsev VM, Yakovleva IL, Karkina LE, Khlebnikov YV, Tabatchikova TI, Urtsev VN. *Russ Phys J* 2004;47:807.
- [43] Janecek M, Louchet F, Doisneau-Cottignies B, Bréchet Y, Guelton N. *Philos Mag A* 2000;80:1605.
- [44] Kobayashi Y, Takahashi J, Kawakami K. *Ultramicroscopy* 2011. doi:10.1016/j.ultramic.2011.01.016.
- [45] Embury JD, Hirth JP. *Acta Metall Mater* 1994;42:2051.
- [46] Waugh AR, Paetke S, Edmonds DV. *Metallography* 1981;14:237.
- [47] Raabe D, Ohsaki S, Hono K. *Acta Mater* 2009;57:5254.
- [48] Raabe D, Choi P, Li YJ, Kostka A, Sauvage X, Lecouturier F. *MRS Bull* 2010;35:982.
- [49] Sinclair CW, Embury JD, Weatherly GC. *Mater Sci Eng A* 1999;272:90.
- [50] Misra A, Hirth JP, Hoagland RG. *Acta Mater* 2005;53:4817.
- [51] Sauvage X, Guelton N, Blavette D. *Scripta Mater* 2002;46:459.